Nanoscale

Accepted Manuscript

This article can be cited before page numbers have been issued, to do this please use: B. Han, S. Chen, J. Zou, R. Shao, Z. Dou, C. Yang, X. Ma, J. Lu, K. Liu, D. Yu, L. Wang, H. Wang and P. Gao, *Nanoscale*, 2019, DOI: 10.1039/C9NR00483A.

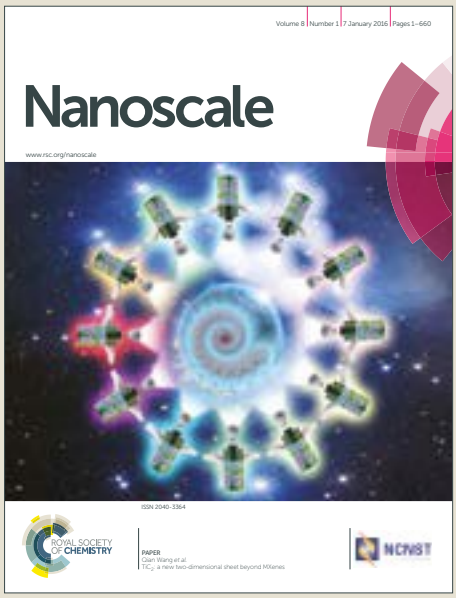

ROYAL SOCIETY OF CHEMISTRY

rsc.li/nanoscale

ROYAL SOCIETY OF CHEMISTRY
View Article Online
DOI: 10.1039/C9NR00483A

Nanoscale

ARTICLE

In situ TEM tracking sodium migration in TiS_2

Bo Han[a,b], Shulin Chen[b,c], Jian Zou[d], Ruiwen Shao[b], Zhipeng Dou[b,e], Chen Yang[f,g], Xiumei Ma[b], Jing Lu[f,g], Kaihui Liu[f,h], Dapeng Yu[b,f,h,i], Liping Wang[d,*], Haicheng Wang[a,*], and Peng Gao[b,h,j*]

Received 00th January 20xx,
Accepted 00th January 20xx

DOI: 10.1039/x0xx00000x

www.rsc.org/

For alkali-metal ion batteries, revealing the phase transformation and the ion migration dynamics in the electrodes is vital to understand how the electrodes work and thereby how we can improve them. Here, by using *in situ* transmission electron microscopy, we track the structural evolution and migration dynamics during sodium insertion into the TiS_2 nanostructures with the lattice fringe resolution. We find that the sodiation process of TiS_2 is initiated by an intercalation reaction and followed by a conversion reaction. From the same reaction event, the velocity of intercalation/conversion phase boundary migration is measured to be ~ 1.0-1.7 nm s^{-1}, while the pristine/intercalation phase boundary migrates at a velocity of ~ 2.5 nm s^{-1}. The sodium migration leads to structure fracture to form nanometer-sized domains (~ 3 nm) with a volume expansion. During migration, Na prefers to transport along specific directions. Furthermore, a superstructured $Na_{0.25}TiS_2$ intermediate phase with ordered Na ions occupied within (0001) plane is formed at the reaction front, which is different from the common staging phase. These findings help us to understand the working principle and the failure mechanism of the sodium ion battery and also provides useful insights into general ionic doping of transition metal dichalcogenide.

Introduction

Lithium-ion batteries (LIBs) have been widely applied in portable electronic devices.[1-4] However, the uneven distribution of lithium on the earth and its limited natural abundance restrict its further application in large-scale energy storage field such as power grid storage and electric vehicles. Therefore, the development of new battery systems other than LIBs is necessary. Na-ion batteries (NIBs) have recently attracted much attention[5-8] due to the low cost, large reserves, wide distribution, less toxic and environmentally friendly properties of sodium.[9-11] Especially, recently it has been demonstrated that the sodium ion battery can also be used to power the electric vehicles.[12] However, finding suitable electrode materials to achieve high power and high capacity is still the main challenge. Compared with LIBs, NIBs are more likely to suffer from voltage hysteresis and relatively poor rate capability due to the larger mass and radius of sodium.[5] Therefore, some high-performance electrode materials in LIBs systems are no longer appropriate for NIBs. As an example, graphite is commonly used as an anode in LIBs but the insertion of sodium ions is impossible in conventional carbonate-based electrolyte systems.[13]

Recently, some of transition metal dichalcogenides (TMDs), which can be generally represented by layered structure AB_2 (A=Mo, Ti, Ta, Hf, W et al; B=S, Se, Te), were applied as electrode materials for sodium ion batteries.[13-17] Since the B-A-B atomic layers of TMDs materials are connected by weak van der Waals forces, the TMDs usually have relatively large lattice space along [0001] direction, which can reversibly accommodate alkali metal ion without excess volume expansion. A host of TMDs, such as MoS_2,[14, 17] SnS_2,[15] WS_2,[16] and low cost TiS_2[18] have been demonstrated to be potential electrode materials in NIB systems for good rate property and stable cyclability. In fact, Winn et al.[19] in 1970s firstly verified that sodium ions could electrochemically insert into TiS_2 host lattice using coulometric titrations, and later in 1980 Newman et al.[20] assembled reversible Na-TiS_2 cells at room temperature and observed the capacity loss at a high voltage upon cycling. As a promising NIB electrode material, the theoretical specific capacity of TiS_2 is 239 mAh/g for intercalation electrochemical reaction to be $NaTiS_2$. Previous electrochemical study showed

[a.] National Center for Materials Service Safety, University of Science and Technology Beijing, Beijing 100083, China
[b.] Electron Microscopy Laboratory, School of Physics, Peking University, Beijing 100871, China
[c.] State Key Laboratory of Advanced Welding and Joining, Harbin Institute of Technology, Harbin 150001, China
[d.] School of Materials and Energy, State Key Laboratory of Electronic Thin Film and Integrated Devices, University of Electronic Science and Technology of China, Chengdu 610054, China
[e.] Key Laboratory for Micro-/Nano-Optoelectronic Devices of Ministry of Education, School of Physics and Electronics, Hunan University, Changsha 410082, China
[f.] State Key Laboratory for Artificial Microstructure & Mesoscopic Physics, School of Physics, Peking University, Beijing 100871, China
[g.] Academy for Advanced Interdisciplinary Studies, Peking University, Beijing 100871, China
[h.] Collaborative Innovation Center of Quantum Matter, Beijing 100871, China
[i.] Shenzhen Key Laboratory of Quantum Science and Engineering, Shenzhen 518055, China
[j.] International Center for Quantum Materials, School of Physics, Peking University, Beijing 100871, China
*Corresponding authors: lipingwang@uestc.edu.cn, hcwang@mater.ustb.edu.cn, and p-gao@pku.edu.cn

View Article Online
DOI: 10.1039/C9NR00487A

that TiS_2 demonstrated a specific capacity of 186 mAh/g at high current rate 100 mAh/g and good cycling stability.[18] To further improve the performance of TiS_2 electrode, revealing the phase transformation and the ion migration behavior is of crucial. The first-principle calculations[21, 22] and nuclear magnetic resonance (NMR) experiments[23, 24] suggested that the behavior of alkali ions migration in TiS_2 are very different than those in the covalent or ionic transition metal oxides with variable valences, mainly due to unique weak van der Waals interactions. In the past decades, a multitude of newly developed techniques including *in situ* X-ray photoelectron spectroscopy (XPS)[25] and *in situ* X-ray diffraction (XRD)[26] have been used to clarify the mechanism of Na-intercalate TiS_2 process. The XRD measurement has shown that an unidentified Na_xTiS_2 phase appeared when TiS_2 was discharged to 1.5 V, while other unknown phases formed in the fully discharged electrode at 0.8 V.[27] However, these commonly used bulk-based techniques collecting information from a large area cannot reveal the intermediate and/or localized phases during reactions, which, indeed, were proposed to exist during alkali ions intercalated within the TiS_2.[28]

Here, phase transformation and dynamic behavior of sodium ions migration in TiS_2 electrode materials is tracked by using high resolution *in situ* transmission electron microscopy (*in situ* TEM) technique.[29-34] We find that the insertion of Na into TiS_2 is initiated by an intercalation reaction then followed by a conversion reaction. The velocity of pristine/intercalation phase boundary migration is ~ 2.5 nm s^{-1}, which is typically larger than the velocity of intercalation/conversion phase boundary ~ 1.0-1.7 nm s^{-1}. The sodium ions insertion leads to the formation of nanosized $Na_{0.25}TiS_2$ domains with local structure ordering, i.e., alternative Na and vacancies within every (0001) plane is detected in the intermediate $Na_{0.25}TiS_2$ phase, which is distinct from the common staging phase that consists of Na and vacancy (0001) plane. The formation of structure ordering is possibly triggered by the existence of the considerable elastic strain induced by sodium ions intercalation and delicate repulsive interactions between them. However, the intermediate superstructured $Na_{0.25}TiS_2$ has not been observed from the *ex situ* experiments, indicating that *in situ* TEM probing with high spatial resolution and temporal resolution can be very useful to acquire the information of structural evolution and ionic migration behavior in solids.

Experimental Section

In situ TEM Experiment

The TiS_2 nanosheets were mechanically exfoliated from a single crystal TiS_2 by using an adhesive tape and then transferred onto a half TEM bare copper grid (without carbon film) by scratching. The Cu grid was home-cut in an argon-filled glove box. The copper grid with TiS_2 was acting as a working electrode. The sodium metal was scratched by a tungsten tip acting as a counter electrode. All of the components were assembled in an electrical TEM specimen holder (PicoFemto) in an argon-filled glove box and then transferred into the TEM chamber. During the transferring, the sodium metal was deliberately exposed to the air (~ 5 s) to coat a thin passivation layer of Na_2O on the sodium metal surface (acting as solid-state electrolyte).[35, 36] To achieve the sodiation process, the sodium metal coated with passivation layer was driven by a piezoelectric ceramic motor to contact with the TiS_2 nanosheet. A small negative bias (~ –2 V) was applied between the tungsten probe and the grounded Cu grid with TiS_2 nanostructures to initiate the reactions.

Electrochemical Measurements

The commercial TiS_2 used for this work was purchased from Alfa Aesar Company. TiS_2 (80 wt. %), carbon black (10 wt. %), polyvinylidene fluoride (PVDF, 10 wt. %) and N-methylpyrrolidone (NMP) were used to fabricate the electrode. We mixed the components to prepare uniform slurry, and then dispersed the slurry onto a copper foil, drying at 80 ° C for 12 h in vacuum environment. 1 M $NaPF_6$ was used as the electrolyte, which was prepared by mixing ethylene carbonate (EC) and dimethyl carbonate (EC: DMC = 50:50 vol%). Sodium foil and glass fiber were used as the anode and the separator, respectively. The weight of the assembled electrode materials was about 2.0 mg cm^{-2}. 2032 coin cells were manufactured in an argon-filled glovebox (O_2 < 0.1 ppm; H_2O < 0.1 ppm). The batteries were galvanostatically discharged and charged at a current density of 100 mA g^{-1} on a LAND CT2001A cell test apparatus at room temperature.

Data Acquisition and Analysis

In situ high-resolution TEM images and selected area electron diffraction (SAED) pattern were recorded by Tecnai F20 equipped with an OneView IS (Gatan) camera, operated at an accelerating voltage of 200 kV. Note that the sodium migration can induce contrast change because of defects formation that changes the diffraction condition. To determine the expansion distance (between the reference position and the edge of nanosheet) in Figure 2, frame series were recorded (10 frames per second) to study the subtle change in the contrast between neighbouring frames during sodiation process. The atomic resolution STEM image was acquired by an aberration-corrected Titan Themis G2 microscope at 80 kV with a beam current of 30 pA, a convergence semi-angle of 25 mrad, and a collection semi-angle snap in the range of 53-260 mrad. The atomistic models were reproduced by VESTA software. Simulated electron diffraction patterns were carried out by Crystalmaker software. The FFT patterns and filtered images were calculated by DigitalMicrograph (Gatan) software. The plots were obtained using Origin 2018.

DFT calculation

We used *ab initio* density functional theory (DFT) to research the stability of $Na_{0.25}TiS_2$ crystal model. The plane-wave basis set and the projector augmented wave (PAW) pseudopotential calculation were used to relax geometry optimization in the Vienna ab initio simulation package (VASP) software. The atomic positions are fully optimized underneath the 0.001 eV/Å maximum force of each atom and the convergence standard of energy on each atom is within 1×10^{-5} eV. In geometric optimizations, the cutoff energy is 500 eV, and *k*-

View Article Online
DOI: 10.1039/C9NR00487A

point mesh is sampled with a separation of about 0.04 Å^{-1} in the Brillouin zone.

Results and discussion

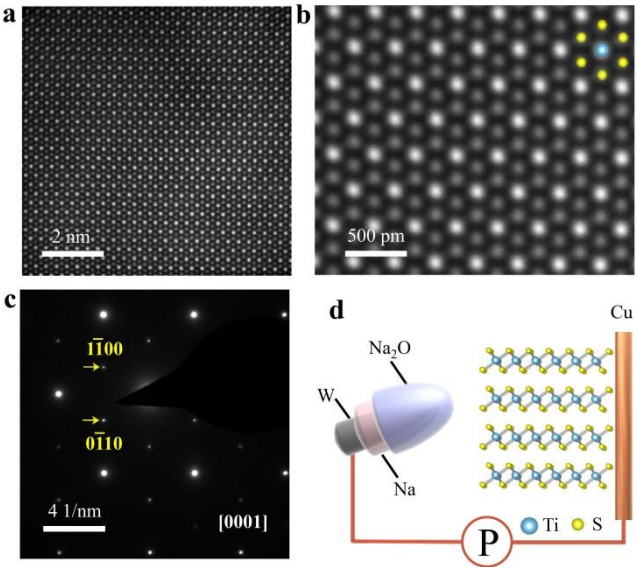

Figure 1. Tracking sodium ion intercalation in TiS_2 nanosheets in real time. (a) An atomically resolved high angle annular dark field scanning transmission electron microscopy (HAADF-STEM) image of TiS_2 viewing from [0001] crystal axis. (b) An atomistic model of TiS_2 unit cell (along [0001] zone axis) overlaid with STEM image. Blue: Ti; yellow: S. (c) Selected area electron diffraction (SAED) pattern of pristine TiS_2 single crystal nanosheet along the [0001] direction. (d) A schematic displays the Na-TiS_2 battery cell assembled in TEM consisting of a TiS_2 nanosheet, a metallic sodium probe and a thin passivation layer of Na_2O acting as solid-state electrolyte.

Figure 1a-b show an atomically resolved high-angle annular dark field scanning transmission electron microscopy (HAADF-STEM) image of the pristine TiS_2 nanosheet viewing from the [0001] direction, where the Ti atoms are brighter than the S atoms because HAADF-STEM image is a Z-contrast (Z is atomic number) image.[37] The SAED viewing from the [0001] zone axis in Figure 1c demonstrates a hexagonal symmetric pattern, which is in agreement with the simulated electron diffraction based on the atomistic model shown in Figure S1 (PDF#15-0853, *a*=3.397 Å, *b*=3.397 Å, *c*=5.691 Å).[38] To observe the Na insertion process in real time, we fabricate a solid-state half-cell in the TEM, consisting of TiS_2 nanosheet, metal sodium counter electrode and Na_2O passivation layer acting as a solid-state electrolyte as shown in Figure 1d and Figure S2.

The sodium-intercalation-induced structural evolution of TiS_2 nanosheet is monitored in Figure 2a (also see movie S1). Na ions insertion can cause lattice distortion and volume expansion. As a result, the strain-induced complex contrast changes are observed in TiS_2 nanosheet during sodiation from the lower magnification images in Figure 2a. The enlarged TEM image in Figure 2b shows that the pristine TiS_2 nanosheet exfoliated from single-crystal TiS_2 has an ordered stacking structure. Note that such stripes are lattice fringes rather than Moiré pattern. A reference position is marked to measure the distance between the reference position and the edge of nanosheet (44.3 nm for pristine). During sodium insertion, the TiS_2 nanosheet begins to swell from 44.3 nm to 71.7 nm (~61.9 % in expansion), as measured in Figure 2c. During this dynamic process, Na insertion breaks the TiS_2 interlayers, forming fractures to release stress and thus accommodate more sodium ions. As a result, the observed volume expansion is significantly larger than the lattice parameter of Na_xTiS_2 ($x \leq 1$) produced by intercalation mechanism.[39] In each small domain of TiS_2 nanosheets, lattice fringes are well preserved and domains are separated by the fractures. As more sodium ions insert into TiS_2 nanosheet, ordered layers finally break up into nanometer-sized domains as shown in Figure 2d. The lengths of the preserved lattices determine the sizes of domains, which are counted in Figure 2e (see Figure S3 for details). The average domain size is measured to be 2.2 ± 1.7 nm. In Figure 2f, we track the structural evolution of a single fracture formation. During the sodium migration, TiS_2 layers start to bend and slide. A straight layer gradually bends and matches with two slid adjacent layers, finally forming a "fork-like" structure at 49.3 s. Such a structure change occurs in all regions where sodium passing through, finally resulting in formation of nanometer size of domains separated by the fractures. The formation of high density of fracture can effectively release the strain caused by sodium ions insertion. Note that the lattice expansion is not caused by beam irradiation and column environment (see details in Figure S4).

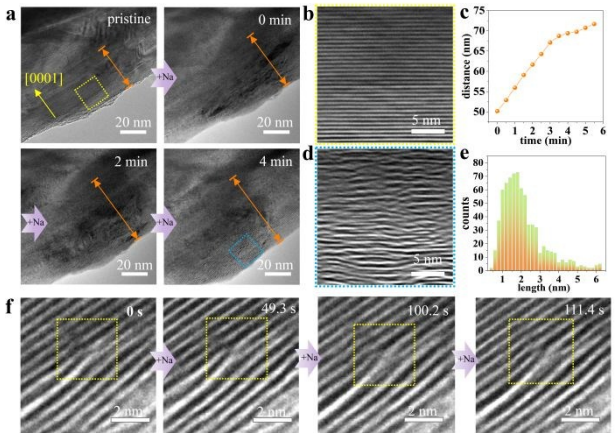

Figure 2. High-resolution TEM tracking of the structural evolution during Na insertion. (a) Selected high resolution TEM image frames showing lattice expansion during Na intercalation (see also in Movie S1). (b) An enlarged view of (a) (squared by the yellow dash line) showing the pristine TiS_2 with viewing direction nearly perpendicular to [0001] zone axis. (c) Distance indicated by orange arrow in (a) is plotted as a function of time, quantitatively illustrating the volume expansion during sodium intercalation. (d) An enlarged view of (a) (squared by the blue dash line) shows the sodiated TiS_2 interlayer. (e) The measured length of nanometer-sized domains of Na-inserted TiS_2. The mean value is measured to be 2.2 ± 1.7 nm. (f) Selected high resolution TEM image series show structural evolution of fracture formation. The drift correct areas are

View Article Online
DOI: 10.1039/C9NR00483A

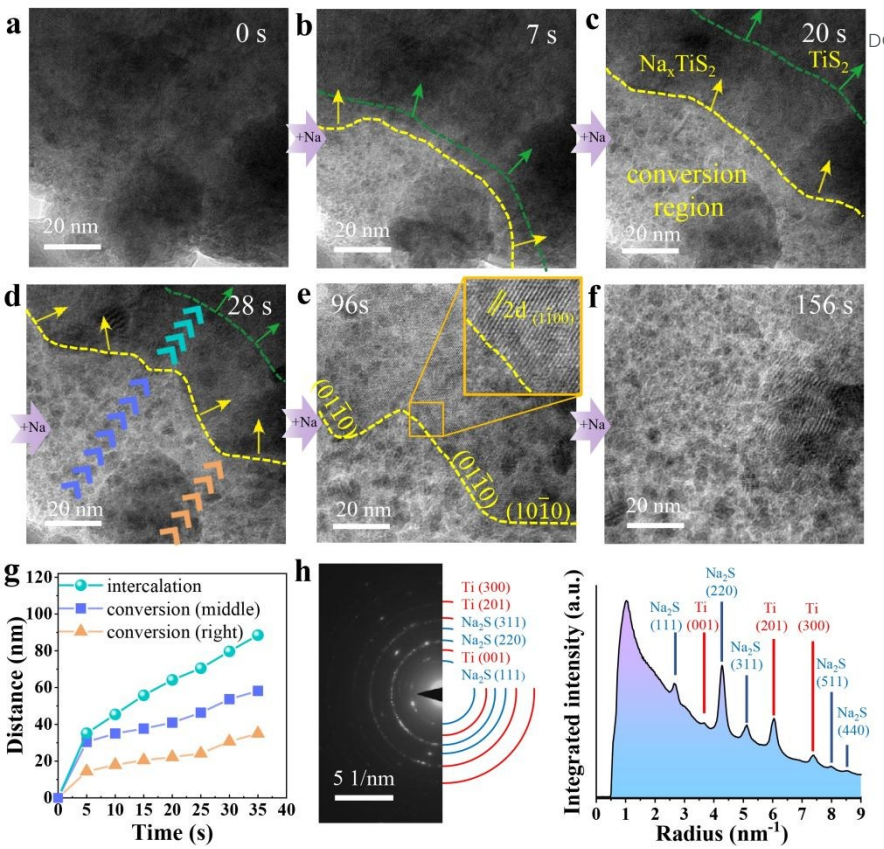

Figure 3. High-resolution TEM tracking of the Na transport in TiS_2 in real time. (a-f) Selected high resolution TEM image series show phase transformation and phase boundary motion process during Na insertion (see also in Movie S2). Yellow dash lines show the boundary between conversion region and Na_xTiS_2 superstructure region while green dash lines indicate the interfaces between superstructure region and initial TiS_2 region. (g) Phase boundary migration distance indicated by sequential arrows in (d) are plotted as a function of time. Intercalation and conversion (middle and right) reaction front are marked by cyan, blue and orange, respectively. (h) A SAED pattern and corresponding radial-integral plot of sodiated TiS_2 electrode of coin cell battery discharged to 0 V.

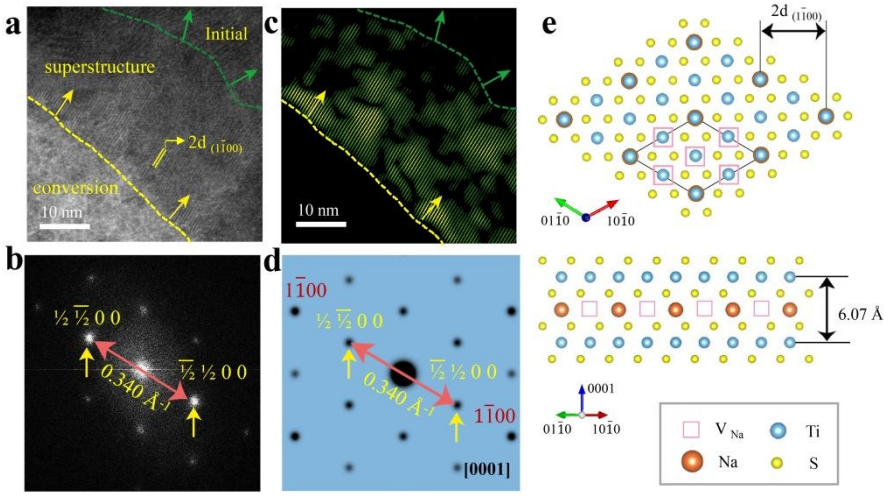

Figure 4. Superstructure of Na-intercalated TiS_2 during sodiation. (a) An enlarged view of high resolution TEM image at 21 s during sodiation. Boundaries between conversion region, Na_xTiS_2 superstructure, and initial region are indicated by yellow and green dash lines, respectively. Arrows show the propagation direction of boundary migration. (b) The FFT pattern of (a), the spacing of superstructure planes are measured (0.340 $Å^{-1}$) as half of {1$\bar{1}$00} in simulated diffraction pattern of pristine TiS_2 (0.680 $Å^{-1}$ in Figure S7b). (c) A filtered image of (a) by using masks to select (½ $\bar{½}$ 00) and ($\bar{½}$ ½ 00) superstructure FFT spots. (d) A simulated electron diffraction pattern of $Na_{0.25}TiS_2$ superstructure. The viewing direction is [001]. (e) An atomic schematic of Na intercalated superstructure optimized by DFT calculation, wherein Na, Ti and S atoms are marked with orange, blue, and yellow balls. Pink squares represent the vacancy between interlayers. One fourth of the interlayer positions are occupied by sodium ions.

The high-resolution TEM image series in Figure 3a-f show the phase boundaries propagation during Na insertion in TiS_2 (also see in movie S2). At the front of reaction, some wide strips come out, representing the generation of an intercalated Na_xTiS_2 phase with superstructure, for which the structure will be discussed later in detail. Interestingly, there are two

View Article Online
DOI: 10.1039/C9NR00483A

interfaces during sodium migration in Figure 3c, i.e., one interface is between the pristine TiS_2 domain and the sodium intercalated Na_xTiS_2 domain, and the other one is between the intercalated domain and conversion domain. Positions of interfaces at different stages are determined from the images filtered in Fourier space by including only the lattice plane frequencies of superlattice in Figure S5. As the reaction goes on, both of the interfaces gradually move forward but they have different propagation velocities. Based on the positions of interfaces, we can estimate the velocities for both intercalation and conversion reactions. The average migration velocities of intercalation/conversion phase boundary are measured to be ~ 1.7 nm s^{-1} (middle) and ~ 1.0 nm s^{-1} (right), while the pristine/intercalation phase boundary migrates at a velocity of ~ 2.5 nm s^{-1}. The migration velocity of Na intercalated phase boundary in TiS_2 is lower than that in MoS_2 (~ 3-7 nm s^{-1}) reported in the previous work.[33] Note that the measured velocity of phase boundary might be primitive as it also depends on the localized contact conditions which can be different from one to another. Nevertheless, these numbers still give us some quantitative information on the comparison of relative diffusivity for intercalation and conversion reactions. For both intercalation and conversion, the reaction velocities decrease after 5 s because the potential field near the probe is larger than that away from the probe. Figure 3e shows the interface between the Na_xTiS_2 domain and the conversion domain prefers to sit in the specific crystal planes $\{10\bar{1}0\}$ likely due to anisotropic barriers for Na transport. After conversion at 156 s, Ti nanoparticles and Na_2S are generated, as shown in Figure 3f. We also study the reactions in realistic battery by *ex situ* TEM method. The sodiated TiS_2 nanosheets from the sodium ion coin battery electrode that discharged to 0 V verify that the fully discharged products are Na_2S and Ti nanocrystalline based on the SAED pattern in Figure 3h and high resolution TEM image in Figure S6.

The structure of intermediated phase Na_xTiS_2 is also identified below. Figure 4a is an enlarged view of TEM image recorded at 20 s. The lattice-spacing of the superstructure phase (0.588 nm) is as twice as the lattice-spacing of $(1\bar{1}00)$ planes for pristine TiS_2 (0.294 nm). The corresponding Fast Fourier Transform (FFT) pattern (Figure 4b) also shows the extra superstructure spots. Based on the FFT filtered image by only including the superstructure reflections in Figure 4c, the spatial distribution of the Na intercalated superstructure phase and the phase boundary can be determined. From the FFT pattern and high resolution TEM image, the intercalated phase is identified to be one sodium occupies the position of every four-unit cell, i.e., a 2×2 ordered superstructure $Na_{0.25}TiS_2$. The simulated electron diffraction pattern (Figure 4d) of $Na_{0.25}TiS_2$ phase is in good agreement with the FFT pattern obtained by experiment. Note that occupation of the S_6 octahedral sites (O1) of interlayers has the lowest energy[40], the atomic structure of $Na_{0.25}TiS_2$ is therefore proposed in Figure 4e. Viewing from $[11\bar{2}0]$ direction, one fourth of the interlayer positions are occupied by sodium ions. The structure stability of the proposed $Na_{0.25}TiS_2$ is further tested and the geometry is also optimized by using density functional theory (DFT) calculations.

In fact, the local structure ordering in alkali metal ions intercalated van der Waals materials such as K-TiS_2[41] and Li-graphite[42, 43] have been reported in previous works. The formation of the superstructure can minimize the elastic strain induced by the sodium intercalation and repulsive interaction between them. These superstructures are called as 'staging phase' consisting of occupied and unoccupied (0001) layers [each (0001) plane is either fully occupied or empty]. However, our observation of $Na_{0.25}TiS_2$ superstructure phase is somehow different from the common staging phase, i.e., Na and vacancy ordering alternatively within each (0001) planes. Also, it was reported that Na prefers to locate in hybrid staged hosts with mixed O1-P3 stacking at low Na concentration ($0.2 < x < 0.25$), i.e., Na ions simultaneously occupy in an octahedral host layer and an adjacent prismatic host layer to form hybrid.[39] However, in our study, under the dominance of kinetic behavior, the insertion of Na leads to an O1 ordering intermediate phase instead of O1-P3 hybrid.

In the case of sodiation in TiS_2, the conversion reaction tends to occur depending on the amount of inserted sodium ions. From in-situ TEM observation, an intercalation reaction firstly occurs, which attributes to a small amount of sodium ions insertion. As more sodium ions insert into TiS_2, the conversion reaction is then triggered. The *ex situ* electrochemical characterizations (Figure S8) also confirm such reactions. At the voltage range of 1-3 V, the TiS_2 electrode can achieve the specific capacity of 184 mAh/g by intercalation mechanism. Once the electrode is discharged to below 1 V, excessive Na ions insert into TiS_2, leading to conversion reaction. Although inserting more Na in Na_xTiS_2 increases the theoretical capacity, the conversion reaction is not fully reversible under real working conditions due to a large volume expansion and formation of amorphous/nanocrystalline, resulting in the capacity fade.[44] Furthermore, as shown in the initial discharge profile from *ex situ* measurements of Na-TiS_2 half battery cell (Figure S8), the plateau at 2.1 V represents the intercalation reaction with Na_xTiS_2 phase generation. However, the $Na_{0.25}TiS_2$ phase with ordered sodium ions is not observed, indicating that the kinetic transformation pathways can fundamentally deviate from the equilibrium phase diagram (thermodynamic phase transition), which can help us to understand the origin of voltage hysteresis in the batteries. In this sense, our *in situ* observations with high spatial resolution and temporal resolution have the advantages to extract the information of structural evolution and ionic migration behavior in solids.

Conclusions

In summary, we use a high resolution *in situ* TEM technique to track the sodium insertion into the TiS_2 nanosheet and both of the intercalation reaction and conversion reaction are observed. At the lattice fringe resolution, we discover that the sodium migration in TiS_2 leads to volume expansion and structure fracture with the formation of nanosized domains (~

3 nm), which should account for the degraded capacities during the following cycling. The pristine/intercalation phase boundary migrates at a velocity of ~ 2.5 nm s^{-1}, which is larger than that of intercalation/conversion phase boundary migration (~ 1.0-1.7 nm s^{-1}). The sodium diffusion is anisotropic, i.e., the interface is preferably along $\{10\bar{1}0\}$ planes, suggesting that anisotropic diffusion barriers.

The sodium intercalated intermediate phase $Na_{0.25}TiS_2$ shows ordering of Na occupation, i.e., within each (0001) plane one fourth of the unit cells are occupied by sodium to form a 2 $\times$ 2 superstructure. The formation of the superstructure can minimize the elastic strain induced by the sodium intercalation and repulsive interaction between them. However, this superstructure is distinct from the common staging phase that consists of Na and vacancy in alternative (0001) planes. From the *ex situ* experiments, Ti nanocrystalline and Na_2S generate when the coin cell is fully discharged, which are in good agreement with the *in situ* TEM results. However, the superstructure phase has not been observed when the battery electrode is discharged to 2.1 V, which is corresponding to $Na_{0.25}TiS_2$, suggesting that the deviation between kinetic transformation pathways and the thermodynamic phase transition is possible. Our direct observations demonstrated in this study can help us to understand the migration process of alkali-metal ions in transition metal dichalcogenides and enlighten the design and development of better sodium ion batteries.

Conflicts of interest

There are no conflicts to declare.

Acknowledgements

The work was supported by the National Key R&D Program of China (2016YFA0300903), the National Natural Science Foundation of China [11771051, 51502007 and 51672007], the National Equipment Program of China (ZDYZ2015-1) and "2011 Program" Peking-Tsinghua-IOP Collaborative Innovation Center of Quantum Matter. We gratefully acknowledge Electron Microscopy Laboratory in Peking University for the use of Cs corrected electron microscope and *in situ* TEM platform.

Notes and references

1 M. Armand and J.-M. Tarascon, *nature*, 2008, **451**, 652.
2 B. Scrosati, J. Solid State Electrochem., 2011, **15**, 1623-1630.
3 R. Service, *Science*, 2018, **359**, 1080.
4 L. Wang, Q. Wang, W. Jia, S. Chen, P. Gao and J. Li, *J. Power Sources*, 2017, **342**, 175-182.
5 M. D. Slater, D. Kim, E. Lee and C. S. Johnson, *Adv. Funct. Mater.*, 2013, **23**, 947-958.
6 D. Kundu, E. Talaie, V. Duffort and L. F. Nazar, *Angew. Chem. Int. Ed Engl*, 2015, **54**, 3431-3448.
7 C. Vaalma, D. Buchholz, M. Weil and S. Passerini, *Nat. Rev. Mater.*, 2018, **3**, 18013.
8 J. Liang, F. Li and H. M. Cheng, *Energy Storage Mater.*, 2017, **7**, A1-A3.
9 D. Larcher and J. M. Tarascon, *Nat Chem.*, 2015, **7**, 19-29.
10 S. Kim, D. Seo, X. Ma, G. Ceder and K. Kang, *Adv. Energy Mater.*, 2012, **2**, 710-721.
11 Y. Wang, R. Chen, T. Chen, H. Lv, G. Zhu, L. Ma, C. Wang, Z. Jin and J. Liu, *Energy Storage Mater.*, 2016, **4**, 103-129.
12 Website:http://www.iop.cas.cn/xwzx/snxw/201806/t20180608_5024146.html.
13 M. M. Doeff, Y. Ma, S. J. Visco and L. C. De Jonghe, *J. Electrochem. Soc.*, 1993, **140**, L169-L170.
14 Z. Hu, L. Wang, K. Zhang, J. Wang, F. Cheng, Z. Tao and J. Chen, *Angew. Chem.*, 2014, **126**, 13008-13012.
15 B. Qu, C. Ma, G. Ji, C. Xu, J. Xu, Y. S. Meng, T. Wang and J. Y. Lee, *Adv. Mater.*, 2014, **26**, 3854-3859.
16 D. Su, S. Dou and G. Wang, *Chem. Commun. (Camb)*, 2014, **50**, 4192-4195.
17 X. Xie, Z. Ao, D. Su, J. Zhang and G. Wang, *Adv. Funct. Mater.*, 2015, **25**, 1393-1403.
18 Y. Liu, H. Wang, L. Cheng, N. Han, F. Zhao, P. Li, C. Jin and Y. Li, *Nano Energy*, 2016, **20**, 168-175.
19 D. A. Winn, J. M. Shemilt and B. C. H. Steele, *Mat. Res. Bull.*, 1976, **11**, 559-566.
20 G. H. Newman and L. P. Klemann, *J. Electrochem. Soc.* , 1980, **127** 2097-2099.
21 A. Van der Ven, J. C. Thomas, Q. Xu, B. Swoboda and D. Morgan, *Phys. Rev. B*, 2008, **78**.
22 A. Van der Ven, J. Bhattacharya and A. A. Belak, *Acc. Chem. Res.*, 2013, **46**, 1216-1225.
23 M. Wilkening, W. Kuechler and P. Heitjans, *Phys. Rev. Lett.*, 2006, **97**.
24 M. Wilkening and P. Heitjans, *Phys. Rev. B*, 2008, **77**.
25 D. Tonti, C. Pettenkofer and W. Jaegermann, *J. Phys. Chem. B* 2004, **108**, 16093–16099.
26 B. Tian, W. Tang, K. Leng, Z. Chen, S. J. R. Tan, C. Peng, G.-H. Ning, W. Fu, C. Su, G. W. Zheng and K. P. Loh, *ACS Energy Lett.*, 2017, **2**, 1835-1840.
27 H. S. Ryu, J. S. Kim, J. S. Park, J. W. Park, K. W. Kim, J. H. Ahn, T. H. Nam, G. Wang and H. J. Ahn, *J. Electrochem. Soc.*, 2012, **160**, A338-A343.
28 A. Leblancsoreau, M. Danot, L. Trichet and J. Rouxel, *Mater. Res. Bull.*, 1974, **9**, 191-197.
29 K. He, S. Zhang, J. Li, X. Yu, Q. Meng, Y. Zhu, E. Hu, K. Sun, H. Yun, X. Q. Yang, Y. Zhu, H. Gan, Y. Mo, E. A. Stach, C. B. Murray and D. Su, *Nat. Commun.*, 2016, **7**, 11441.
30 Z. Zeng, X. Zhang, K. Bustillo, K. Niu, C. Gammer, J. Xu and H. Zheng, *Nano Lett.*, 2015, **15**, 5214-5220.
31 H. Xie, X. Tan, E. J. Luber, B. C. Olsen, W. P. Kalisvaart, K. L. Jungjohann, D. Mitlin and J. M. Buriak, *ACS Energy Lett.*, 2018, **3**, 1670-1676.
32 M. E. Holtz, Y. Yu, D. Gunceler, J. Gao, R. Sundararaman, K. A. Schwarz, T. A. Arias, H. D. Abruna and D. A. Muller, *Nano Lett.*, 2014, **14**, 1453-1459.
33 P. Gao, L. Wang, Y. Zhang, Y. Huang and K. Liu, *ACS nano*, 2015, **9**, 11296-11301.
34 P. Gao, Y.-Y. Zhang, L. Wang, S. Chen, Y. Huang, X. Ma, K. Liu and D. Yu, *Nano Energy*, 2017, **32**, 302-309.
35 J. W. Wang, X. H. Liu, S. X. Mao and J. Y. Huang, *Nano Lett.*, 2012, **12**, 5897-5902.
36 M. Gu, A. Kushima, Y. Shao, J. G. Zhang, J. Liu, N. D. Browning, J. Li and C. Wang, *Nano Lett.*, 2013, **13**, 5203-5211.
37 S. Pennycook and D. Jesson, *Ultramicroscopy*, 1991, **37**, 14-38.
38 I. Oftedal, *Zeitschrift für Physikalische Chemie*, 1928, **134**, 301-310.
39 T. Hibma, *J. Solid State Chem.*, 1980, **34**, 97-106.

View Article Online
DOI: 10.1039/C9NR00483A

40 J. Vinckeviciute, M. D. Radin and A. Van der Ven, *Chem. Mater.*, 2016, **28**, 8640-8650.
41 L. Wang, J. Zou, S. Chen, G. Zhou, J. Bai, P. Gao, Y. Wang, X. Yu, J. Li, Y.-S. Hu and H. Li, *Energy Storage Mater.*, 2018, **12**, 216-222.
42 J. E. Fischer and T. E. Thompson, *Phys. Today*, 1978, **31**, 36-45.
43 W. Rudorff, *Adv. Inorg. Chem.*, 1959, **1**, 223-266.
44 H. Tao, M. Zhou, R. Wang, K. Wang, S. Cheng and K. Jiang, *Adv. Sci.*, 2018, **5**, 1801021.

View Article Online
DOI: 10.1039/C9NR00483A

Graphical Abstract

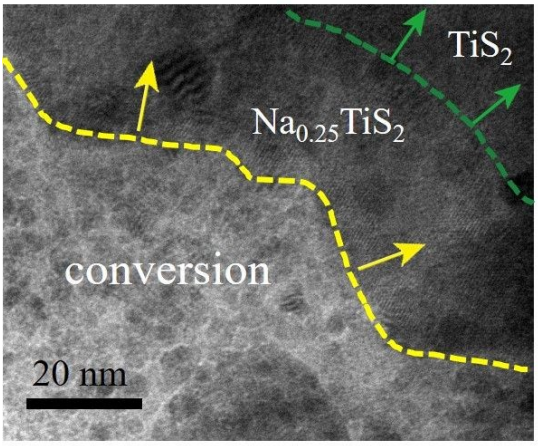

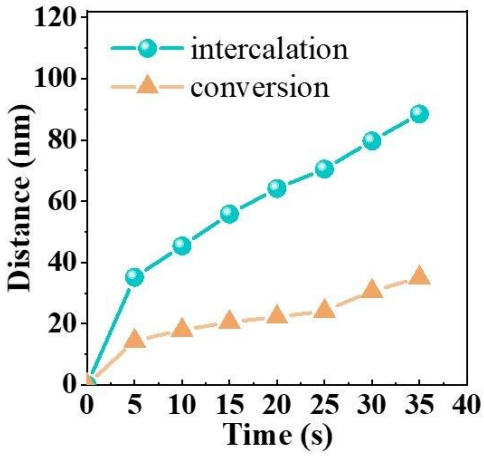

by using *in situ* TEM, the structural evolution and migration dynamics are revealed during sodium migration in TiS_2